

Near-Field-Focusing Integrated Optical Phased Arrays

Jelena Notaros , *Student Member, IEEE*, Christopher V. Poulton , *Member, IEEE*,
Manan Raval, *Student Member, IEEE*, and Michael R. Watts, *Member, IEEE*

Abstract—Integrated optical phased arrays that focus radiated light to a tightly-confined spot in the near field are demonstrated for the first time. The element phase distributions necessary for generating and steering focused beams using phased arrays are developed. Discussion and simulations detailing the effects of the array aperture and focal length on the focal spot are included. Two focusing phased array architectures are presented: (1) a one-dimensional splitter-tree-based architecture with novel focusing antennas and inline phase bumps and (2) a two-dimensional large-scale pixel-based architecture. Both architectures are used to experimentally demonstrate a variety of aperture size and focal length passive focusing arrays in a CMOS-compatible platform, including (i) a 512-antenna splitter-tree-based array with a wavelength-steerable 7 μm spot at a 5 mm focal length, (ii) a 1024-antenna pixel-based array with a 21 μm spot at a 5 mm focal length, and (iii) a 10,000-antenna pixel-based array with a 21 μm spot at a 10 mm focal length. The demonstrated focusing phased arrays present a new functional modality compared to standard optical phased arrays that generate diffracting beams in the far field of the array. This new focusing modality has the potential to advance a number of important application areas at the cutting edge of lightwave technology, as it will enable future integrated optical phased array implementations for a wide range of applications that require focusing operation. Such areas include optical trapping for biological characterization, laser-based three-dimensional printing, short-range light detection and ranging, and short-range optical data communications.

Index Terms—Integrated optical phased arrays, photonic integrated circuits, silicon photonics.

I. INTRODUCTION

INTEGRATED optical phased arrays [1]–[12] have emerged as a promising technology for many applications, such as light detection and ranging (LiDAR) [1], projection systems [2], and free-space optical data communications [3], due to their

Manuscript received August 4, 2018; revised October 10, 2018; accepted November 4, 2018. Date of publication November 9, 2018; date of current version November 29, 2018. This work was supported in part by the Defense Advanced Research Projects Agency (DARPA) E-PHI Program under Grant HR0011-12-2-0007 and in part by the National Science Foundation (NSF) Graduate Research Fellowship Program (GRFP) under Grant 1122374. (*Corresponding author: Jelena Notaros.*)

J. Notaros, M. Raval, and M. R. Watts are with the Research Laboratory of Electronics, Massachusetts Institute of Technology, Cambridge, MA 02139 USA (e-mail: notaros@mit.edu; mraval@mit.edu; mwatts@mit.edu).

C. V. Poulton was with the Research Laboratory of Electronics, Massachusetts Institute of Technology, Cambridge, MA 02139 USA, and is currently with Analog Photonics LLC, Boston, MA 02210 USA (e-mail: cpoulton@analogphotonics.com).

Color versions of one or more of the figures in this paper are available online at <http://ieeexplore.ieee.org>.

Digital Object Identifier 10.1109/JLT.2018.2880462

ability to manipulate and dynamically steer light in a compact-form-factor, low-cost, and non-mechanical way. Motivated by these initial applications, optical phased array demonstrations to date have primarily focused on systems that form and steer beams or project arbitrary radiation patterns in the far field of the array [1]–[10].

However, many potential applications of optical phased arrays require focused spots in the near field of the array (as typically generated by bulk-optics lenses) instead of diffracting beams or patterns in the far field (as generated by standard phased arrays). For example, optical trapping and tweezing – the manipulation of particles through non-contact forces for biological characterization [13]–[15] and trapped ion quantum computing [16] – require tightly-focused spots since optical forces are formed due to intensity gradients. Similarly, high-resolution three-dimensional printing using laser-based additive manufacturing is dependent on high-intensity focused spots to enable small voxel sizes [17]. Furthermore, for short-range LiDAR or data communications with targets or receivers within the near-field of the transmitter array, focusing the signal on the object under test or receiver as opposed to forming a diffracting beam in the direction of the target would improve the overall system efficiency.

Typically, focusing beams have been generated using free-space methods, such as conventional and Fresnel bulk-optics lenses, focusing spatial light modulators [18], and metamaterial-based lenses [19], which generally provide diffraction-limited spots at a variety of designed focal lengths. However, these numerous potential applications would benefit from the waveguided compact form-factors [10], low-cost wafer-scale production [1], monolithically-integrated light sources [20], and high-speed dynamic steering capabilities [2] that focusing integrated optical phased arrays could provide while maintaining required performance with large scalable aperture sizes (and, consequently, large focal lengths and small spot sizes) [4]. (To date, near-field optical phased array manipulation has only been theoretically explored for holographic applications [11] and experimentally demonstrated for one-dimensional Bessel-beam generation [12].)

In this paper, Fresnel-lens-inspired focusing integrated optical phased arrays are demonstrated for the first time. Foremost, the phase distributions necessary for generating focused beams are derived, and discussion and simulations detailing the effect of the array aperture and focal length on the full-width half-maximum (FWHM) of the focal spot are included. Additionally, the effect of conventional linear steering on the focal

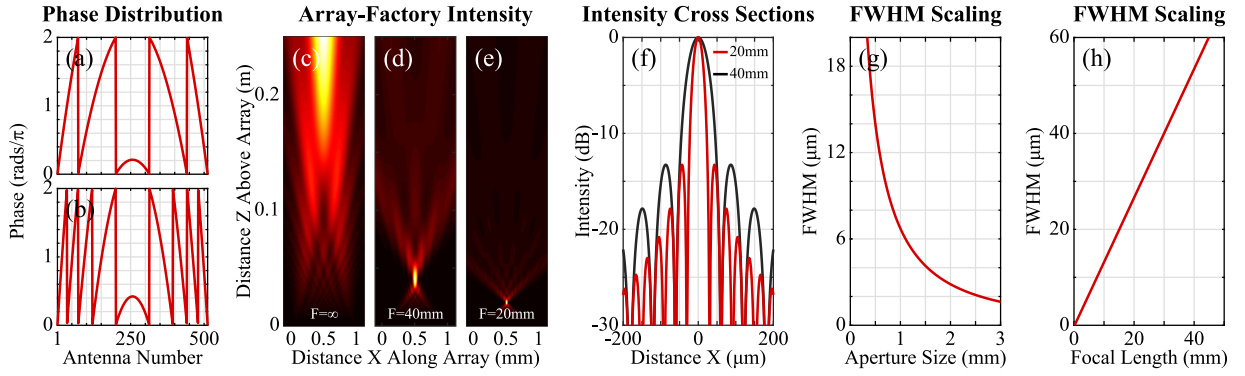


Fig. 1. Element phase distribution for a focusing phased array with (a) 40 mm and (b) 20 mm focal length. Simulated array-factor intensity above the array for (c) a non-focusing, (d) 40 mm focal length, and (e) 20 mm focal length phased array. (f) Simulated cross-sectional array-factor intensity at the focal plane for the 40 mm focal length (black) and 20 mm focal length (red) phased array. Phase profiles and simulated intensities are shown for an array with 512 antennas, 2 μm antenna pitch, and 1550 nm wavelength. (g) Simulated power full-width half-maximum (FWHM) versus aperture size for a focusing phased array with 5 mm focal length and 1550 nm wavelength. (h) Simulated power FWHM versus focal length for a focusing phased array with 1 mm aperture size and 1550 nm wavelength.

length is shown and a modified non-linear steering phase is derived. Next, two architectures are proposed for experimentally demonstrating focusing integrated optical phased arrays. First, a one-dimensional (1D) splitter-tree-based phased array architecture [4] is modified to enable passive near-field focusing in two dimensions. The architecture consists of a 1D splitter tree to evenly distribute the input light to the antenna array, a novel phase bump device before each antenna to passively encode arbitrary phase distributions to the elements of the array and enable focusing in the array dimension, and the first millimeter-scale focusing grating-based antennas to enable focusing in the antenna dimension. This splitter-tree-based architecture is implemented to demonstrate a 512-antenna integrated phased array with a 1.024 mm \times 0.9 mm aperture that focuses light down to a $\sim 7 \mu\text{m}$ spot 5 mm above the chip. Additionally, experimental data showing wavelength steering of the focal spot in the antenna dimension is shown and discussion on extension of the architecture to electronic control in the array dimension is presented. Next, a two-dimensional (2D) pixel-based architecture [5] is utilized to show a second type of passive focusing phased array with the potential for active electronic focusing in two dimensions. This pixel-based architecture consists of a 2D grid of pixels with each pixel passively encoding the amplitude and phase of the light radiated by a compact antenna emitter using a directional coupler and a waveguide offset, respectively. Specifically, a 1024-antenna variant with 32 rows by 32 columns and a 0.32 mm \times 0.32 mm aperture is demonstrated that focuses light to a $\sim 21 \mu\text{m}$ spot 5 mm above the chip, and a 10,000-antenna variant with 100 rows by 100 columns and a 1 mm \times 1 mm aperture is demonstrated that focuses light to a $\sim 21 \mu\text{m}$ spot 10 mm above the chip. By using a CMOS-compatible platform for both architectures, the systems are naturally scalable to active demonstrations with wafer-scale 3D-bonded electronics [21] and monolithically-integrated lasers [20] for a fully-integrated and steerable chip-based source of focused light.

II. FOCUSING PHASED ARRAY THEORY

In general, a phased array is a system comprised of an array of antennas that are fed with controlled phases and amplitudes to

generate arbitrary radiation patterns. If the antennas are spaced with a uniform pitch, d , and fed with a uniform amplitude and a linear phase distribution, the array creates a steerable, diffracting beam in the far field of the array. The near-field electric-field profile generated by this phased array can be approximated using a quasi-array-factor model for the near field (analogous to standard array-factor simulations in the far field):

$$E(x, y, z) = \sum_{n=1}^N E_n(x, y, z) \approx \sum_{n=1}^N A_n e^{-i(2\pi r_n / \lambda + \Phi_n)} \quad (1)$$

where N is the total number of antennas in the array, A_n is the amplitude applied to the n th antenna, Φ_n is the phase applied to the n th antenna, r_n is the distance from the n th antenna to the point under consideration at coordinate (x, y, z) , and λ is the propagation wavelength. Using this method, a standard array with $N = 512$, $d = 2 \mu\text{m}$, and $\lambda = 1550 \text{ nm}$ is simulated; the generated intensity profile is shown in Fig. 1(c).

In contrast, if a “lens-like” hyperbolic element phase distribution is applied, the array will focus light into a tightly-confined spot in the near field above the array. This element phase is derived by calculating the relative delay necessary such that constructive interference of the wavefronts occurs at the focal point. First, the distance from each antenna to the focal point is calculated as:

$$L_n = \sqrt{f_z^2 + d^2 (N/2 + 1/2 - n)^2} \quad (2)$$

where f_z is the desired focal length. To enforce the focusing condition, the phase applied to each antenna should compensate for the differences in the corresponding optical path lengths such that the wavefronts at the focal point constructively interfere. This gives the desired feeding phase distribution

$$\Phi_n = \frac{2\pi}{\lambda} (L_1 - L_n). \quad (3)$$

Similarly to a Fresnel lens, this phase can be encoded modulo 2π , as shown in Figs. 1(a)–(b). This wrapped phase encoding is utilized so that any potential fabrication-induced phase variations in the array will not compound over more than 2π . As such, the system is very robust to phase variations in the array dimension; variations will result in minimal power loss in the focal

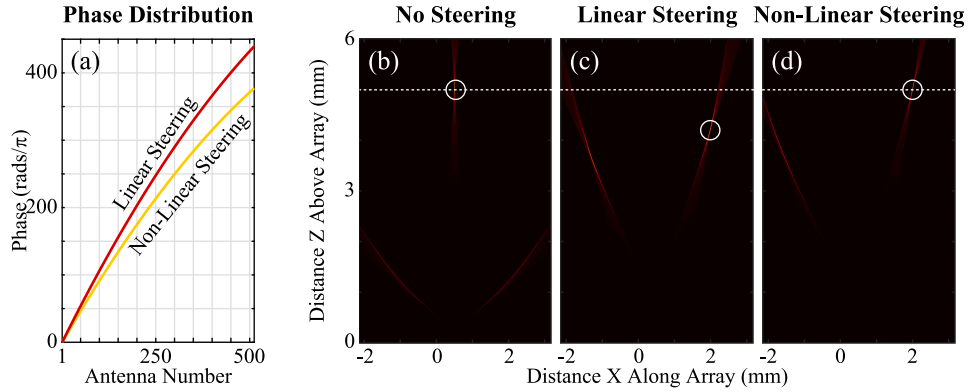


Fig. 2. (a) Element phase distribution for a focusing phased array with an $f_x = 1.5$ mm offset assuming linear steering (red) and corrected non-linear steering (yellow). Simulated array-factor intensity above the array assuming (b) no steering, (c) linear steering, and (d) corrected non-linear steering. Phase profiles and simulated intensities are shown for an array with 512 antennas, $2 \mu\text{m}$ antenna pitch, 5 mm focal length, and 1550 nm wavelength.

spot as opposed to causing displacement of the spot. Additionally, the wrapped phase encoding requires less relative phase difference between antennas, which enables shorter, smaller, and more-fabrication-tolerant phase delay structures for both splitter-tree-based and pixel-based phased array architectures.

Figures 1(d)–(f) show the simulated intensity profiles generated by two focusing phased arrays with $N = 512$, $d = 2 \mu\text{m}$, $\lambda = 1550$ nm, and varying focal lengths. As shown, by applying the derived element phase profiles, the arrays focus light to tightly-confined and highly-enhanced spots. Additionally, due to discretization of continuous theory onto arrays with $d > \lambda/2$, higher-order grating lobes, which also exhibit focusing properties, are generated by the arrays at larger angles (not shown in the simulation windows).

For appreciable focusing, the desired focal length of a focusing array should be limited to the Fresnel region (i.e., the near field) of the phased array, $r_{\text{near}} \approx A^2/\lambda$ where $A = Nd$ is the array aperture size, as given by antenna theory. Consequently, by increasing the aperture size, the possible focal length of the array quadratically increases.

Additionally, for potential applications that require highly-enhanced and tightly-focused spots, a valuable figure of merit of a focusing array is the power FWHM of the resulting spot at the desired focal length. For example, for a 512-antenna array with $2 \mu\text{m}$ antenna pitch at a 1550 nm wavelength, as simulated in Figs. 1(d)–(f), the FWHM is found to be $53.5 \mu\text{m}$ and $26.6 \mu\text{m}$ for focal lengths of 40 mm and 20 mm, respectively.

Similarly to bulk lenses, the FWHM depends on the aperture size of the array and the focal length. As shown in Fig. 1(g), as the array aperture size increases, the FWHM decreases with an inverse scaling. In contrast, as shown in Fig. 1(h), as the desired focal length increases, the FWHM increases linearly. These relationships match with the well-known Rayleigh criterion derived from the Airy pattern, which describes the resolution limit of an imaging system as $R \approx \lambda f_z/A$ where R is the spatial resolution (analogous to the FWHM). As such, for maximally-enhanced focusing at long focal lengths, large aperture sizes are necessary.

One advantage of using integrated optical phased arrays for focused-light applications is that phased arrays allow for dynamic steering on-chip to enable high-speed arbitrary manipu-

lation. In a standard phased-array system, a linear phase gradient is applied to the antennas to steer the radiated beam in the far field [1], [2], [5]–[7]. However, when this conventional linear steering approach is applied to a focusing phased array, in addition to the desired steering in the array dimension, the steering induces an undesired offset to the focal length of the spot. As an example, an array with 512 antennas, $2 \mu\text{m}$ antenna pitch, 5 mm desired focal length, and 1550 nm wavelength is simulated, as shown in Fig. 2(b). When this array is steered to a 1.5 mm offset in the array dimension using linear steering, as shown in Fig. 2(c), the resulting focal spot is formed at $z = 4.19$ mm. For many applications, this steering-induced shift in the focal length can prove to be detrimental; for example, for optical trapping applications wherein the sample under test is often housed in a flat microfluidic channel [13], this effect can shift the focal spot out of the channel.

Instead, the desired horizontal offset should be encoded directly in the focusing phase as follows. First, the distance from each antenna to the focal point, initially given by (2), is modified as:

$$L_n = \sqrt{f_z^2 + [d(N/2 + 1/2 - n) + f_x]^2} \quad (4)$$

where f_z is the desired focal length and f_x is the desired focal offset. The necessary element phase distribution then follows directly from (3). For comparison, the linear and non-linear steering phases are shown in Fig. 2(a) without 2π phase wrapping for clarity. By applying this non-linear steering approach for $f_x = 1.5$ mm, the focal spot is formed with the correct offset at the desired 5 mm focal length, as shown in Fig. 2(d). Note that, similar to a standard beam-forming phased array, as the array is steered, the array's effective area is changed, which, in turn, increases the FWHM of the focal spot from $6.6 \mu\text{m}$ to $7.6 \mu\text{m}$.

III. SPLITTER-TREE-BASED ARCHITECTURE, IMPLEMENTATION, AND EXPERIMENTAL DATA

As a proof of concept, a passive focusing integrated optical phased array is designed and fabricated, as shown in Fig. 3. The phased array architecture utilized in the demonstration is based on a one-dimensional silicon-based splitter tree (similar

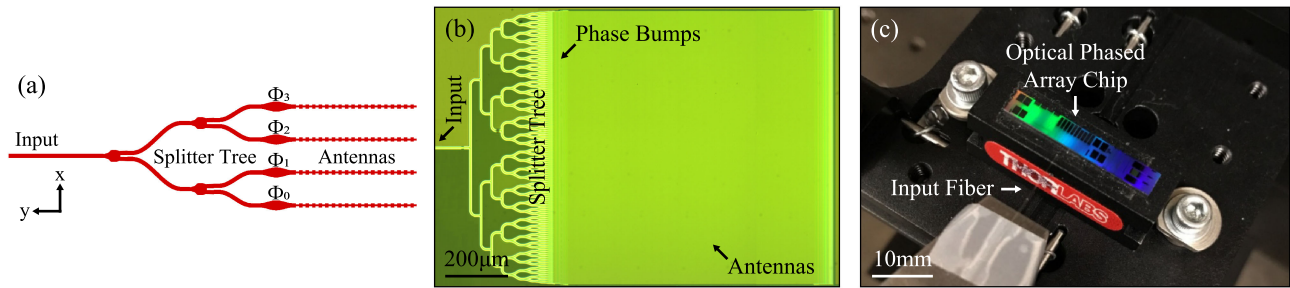


Fig. 3. (a) Schematic of a splitter-tree-based focusing phased array with 4 antennas. (b) Micrograph of a fabricated splitter-tree-based focusing phased array with 512 antennas and 2 μm antenna pitch. (c) Photograph of a fabricated integrated optical phased array chip on the scanning optical imaging setup.

to the silicon-nitride tree architecture demonstrated in [4]) with additional novel phase components and focusing antennas added to enable focusing in the array and the antenna dimensions, respectively.

The phased array and accompanying device test structures are fabricated in a CMOS-compatible foundry process at CNSE SUNY on a 300-mm silicon-on-insulator (SOI) wafer with a 2- μm -thick buried oxide. The 220-nm-thick silicon device layer is patterned using 193 nm immersion lithography.

At the system input, an on-chip inverse-taper edge coupler is designed to efficiently couple light from a 6.5- μm -mode-field-diameter lensed fiber to a 400-nm-wide silicon waveguide with a ~ 2.5 dB measured coupling efficiency.

Next, a 9-layer splitter tree network is used to evenly distribute the input power to 512 waveguide arms with a final pitch of 2 μm . Within the network, a compact Y-junction is used as a symmetric 1-to-2-waveguide splitting device, as developed in [22]. The Y-junction devices are connected by either 90° bends or sinusoidal-shaped bends with 5 μm minimum bending radii to reduce bending radiation loss. The final waveguide pitch is limited to 2 μm to reduce undesired evanescent coupling between antennas in the array.

At the output of the splitter tree, a phase bump structure is placed on each waveguide arm to impart a static phase delay dependent on the maximum width of the device. The phase bump adiabatically increases the width of the waveguide from the nominal 400 nm width to a variable wider width using a sinusoidal shape. The length of the structure is chosen to be 6 μm to reduce undesired excitation of higher-order modes while keeping a compact form factor. As shown in Fig. 4(a) both numerically using a finite-difference time-domain (FDTD) solver and experimentally, as the width of the device is increased, the relative phase induced by the structure increases. As such, by choosing the appropriate widths for each phase bump, the correct phase profile, given by (3), is applied. Note that, due to the robustness of this wrapped phase encoding, the discrepancy between the simulated and measured phase shown in Fig. 4(a) (which can be attributed to discrepancy between the expected and actual fabricated silicon device layer thickness) does not have a significant effect on the resulting performance of the system.

Finally, after each phase bump, a 0.9-mm-long grating-based focusing antenna is placed on each arm to create a

1.024 mm \times 0.9 mm aperture size. The antenna utilizes a full-etch perturbation geometry, similar to [1], to enable radiation out of the plane of the chip. By manipulating the symmetric inward perturbation of each period of the antenna, the local scattering strength, defined as the power radiated by the antenna per unit length, can be controlled, as shown in Fig. 4(b) numerically and experimentally (the discrepancy between simulated and measured values can be attributed to rounding of the perturbations during fabrication without optical-proximity-correction techniques). As such, the antenna is designed with uniform perturbations along the antenna length – i.e., constant scattering strength – to generate an exponentially-decaying intensity profile. Specifically, a 30 nm perturbation is chosen to minimize the excess power at the end of the 0.9-mm-long antenna while maintaining a large effective aperture.

Next, to enable focusing in the antenna dimension, the period of the antenna is adiabatically chirped along the antenna length. This process is similar to adiabatic synthesis of locally periodic vertical grating couplers with varying radiation angles [23]–[25]. To implement this synthesis, the relative phase induced by a single period unit cell of the antenna is simulated in FDTD as the length of the wider, unperturbed section of the antenna is varied and the length of the narrower, perturbed section is kept at a constant 310 nm, as shown in Fig. 4(c). These period unit cells are then chosen and concatenated such that the synthesized phase along the antenna follows the unwrapped phase given by (3). The synthesized lengths for focusing at 1 mm, 5 mm, and 10 mm are shown in Fig. 4(d). Note that an unperturbed section length of 295 nm is chosen as the reference phase point during the synthesis since, at that point, the antenna radiates upwards with a slight angle. Although this introduces a slight angle offset to the beam in the antenna dimension, it ensures that the antenna does not induce undesired back reflections as dictated by the Bragg condition. Additionally, since the focusing antenna is synthesized using the unwrapped phase, it is more susceptible to compounded fabrication-induced phase errors, which can result in undesired variations in the focal spot location and size. Generally, fabrication variations will have a more significant effect on the spot size of antennas with shorter focal lengths and on the focal length of antennas with larger focal lengths.

To characterize the fabricated array, an optical system is used to simultaneously image the plane of the chip onto a visible camera and an InGaAs IR camera. The height of the optical

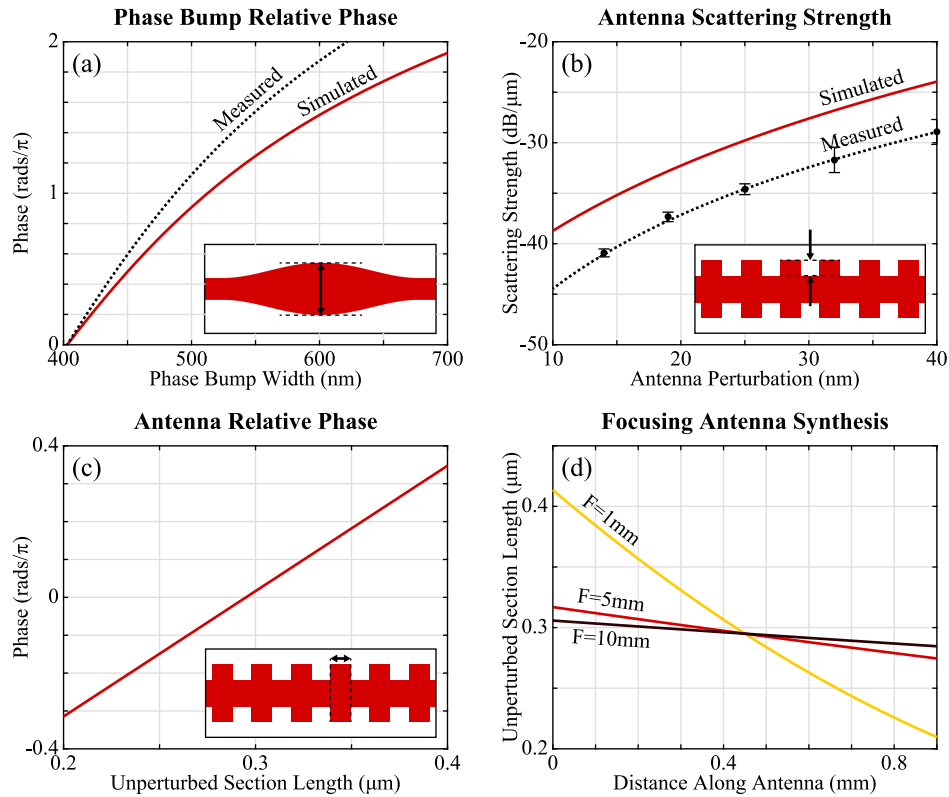


Fig. 4. Simulated (red) and measured (black) (a) relative phase versus phase bump width, (b) scattering strength versus antenna perturbation, and (c) relative phase versus length of the unperturbed section of the antenna. Device schematics are included as insets with each variable parameter indicated. (d) Synthesized unperturbed section length versus distance along the antenna necessary for focusing at 1 mm (yellow), 5 mm (red), and 10 mm (black) for a focusing antenna with a constant 30 nm perturbation and 310 nm perturbed length.

imaging system is then progressively scanned such that top-down views of the intensity at varying heights above the chip are recorded. These top-down views are then integrated in the antenna or the array dimension to visualize the cross-sectional intensity as a function of the distance above the chip.

The resulting cross-sectional intensity as a function of the distance above the chip and three top-down views are shown in Figs. 5(a)–(e) for the fabricated splitter-tree-based 2D-focusing phased array with 512 antennas, 2 μm antenna pitch, 5 mm focal length, and 1550 nm wavelength. In the plane of the chip (Fig. 5(e)), the aperture is illuminated by the antennas. As the system scans to the expected focal plane 5 mm above the chip (Figs. 5(d) and 5(f)), the radiated light is tightly-focused in both the x and y dimensions. At this height, a FWHM of $\sim 6.4 \mu\text{m}$ is measured in the array dimension, x , closely matching the simulated value of 6.6 μm . Similarly, a FWHM of $\sim 7.6 \mu\text{m}$ is measured in the antenna dimension, y , matching the expected value of 7.6 μm . A side-lobe suppression of $\sim 9.5 \text{ dB}$ is measured with an approximately symmetric pattern in the array dimension and an asymmetric pattern in the antenna dimension due to the exponentially-decaying intensity profile of the antennas (note that the noise floor in Fig. 5(f) is limited by the IR camera, not the array itself). Additionally, as expected, the angle in the antenna dimension is slightly offset. Finally, above the focal plane (Fig. 5(c)), the light is, once again, diffracted out. Next, using a pinhole shutter at the focal plane to block any

grating lobes and stray light and a detector above the shutter, an on-chip input to main lobe efficiency of approximately -12 dB is measured (the losses can be attributed to waveguide propagation loss, Y-junction splitter losses, and antenna emission losses, including power radiated to the grating lobes).

For comparison, a similar 1D-focusing array is also fabricated. The array utilizes the same splitter-tree-based architecture with 512 antennas, 2 μm antenna pitch, 5 mm focal length, and 1550 nm wavelength to focus in the array dimension; however, standard non-focusing antennas are used such that the system does not focus in the antenna dimension. The resulting cross-sectional intensity as a function of the distance above the chip and three top-down views are shown in Figs. 5(g)–(j). In the plane of the chip (Fig. 5(j)), the aperture is illuminated by the antennas. As the system scans to the expected focal plane 5 mm above the chip (Fig. 5(i)), the light is tightly-focused in the array dimension to a FWHM of $\sim 6.4 \mu\text{m}$, which closely matches both the simulated and 2D-focusing results. Finally, above the focal plane (Fig. 5(h)), the light is, once again, diffracted out in the array dimension.

Similarly, both 1D- and 2D-focusing phased arrays are also fabricated with a 1 mm focal length. The resulting focal spots have measured FWHMs of $\sim 1.7 \mu\text{m}$ in the array dimension and $\sim 2.9 \mu\text{m}$ in the antenna dimension, compared to the simulated values of 1.4 μm and 1.5 μm , respectively. These slight discrepancies can be attributed to experimental error in measuring such

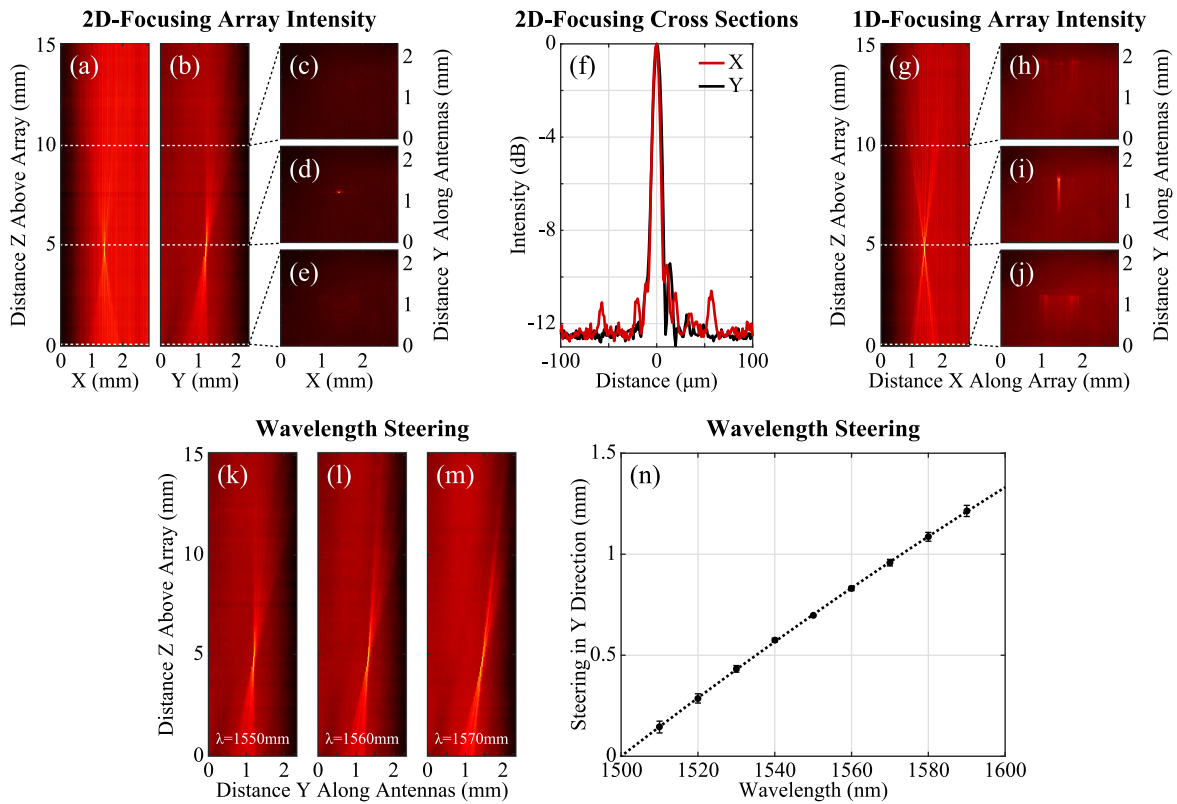


Fig. 5. Measured cross-sectional intensity (in dB) above the chip for a 2D-focusing splitter-tree-based phased array in the (a) x plane and (b) y plane with top-down intensity shown (e) in the plane of the chip, (d) at the focal plane, and (c) above the focal plane. (f) Measured cross-sectional intensity in x (red) and y (black) at the focal plane for the 2D-focusing splitter-tree-based phased array. (g) Measured cross-sectional intensity (in dB) above the chip for a 1D-focusing splitter-tree-based phased array with top-down intensity shown (j) in the plane of the chip, (i) at the focal plane, and (h) above the focal plane. Measured cross-sectional intensity (in dB) above the chip for a 2D-focusing splitter-tree-based phased array at (k) 1550 nm, (l) 1560 nm, and (m) 1570 nm wavelengths. (n) Experimental results showing steering in the antenna dimension, y , versus wavelength. Results are shown for arrays with 512 antennas, 2 μm antenna pitch, and 5 mm focal length.

small spot sizes with the finite pixel size of the IR camera and compounding fabrication-induced phase errors in the focusing antennas.

Finally, the wavelength of the light coupled into the 5-mm-focal-length 2D-focusing array is swept to demonstrate wavelength steering in the antenna dimension. In theory, since the antennas are based on grating principles, as the wavelength of light is increased, the effective period of the antenna becomes smaller and the angle of the light radiated by the antenna varies such that the beam is steered closer to the input of the chip. Three cross-sectional intensities in the antenna dimension for wavelengths of 1550 nm, 1560 nm, and 1570 nm are shown in Figs. 5(k)–(m). As expected, as the wavelength is increased, the radiation angle is shifted while still maintaining its focusing characteristics. To quantify this shift, the spatial offset of the beam in the antenna dimension is plotted as a function of the input wavelength, as shown in Fig. 5(n).

Since the array is fabricated in a CMOS-compatible platform, it is naturally scalable to a dynamic arbitrarily-tunable system with active silicon-based phase shifters on each waveguide arm [2], [4], [6], [8]–[10]. This extension of the system would enable steering of the focal spot in the array dimension in addition to the wavelength steering capability in the antenna dimension. However, although the array-dimension tuning would

be fully arbitrary, this architecture is fundamentally limited to 2D-focusing in only one focal plane since the wavelength steering is only capable of inducing a lateral offset. For applications where both focal length and offset tuning are required, a different architecture capable of scaling to non-linear electrical tuning in both dimensions (as described in Section IV) is necessary.

IV. PIXEL-BASED ARCHITECTURE, IMPLEMENTATION, AND EXPERIMENTAL DATA

Next, as a second method for experimentally demonstrating focusing integrated optical phased arrays, a passive focusing phased array using a two-dimensional pixel-based architecture is designed and fabricated, as shown in Fig. 6(a)–(b). By using the architecture developed in [5], [26] and applying it to the focusing theory developed in Section II, this system is capable of scaling to electrical phase control in both dimensions of the array to enable dynamic tuning of the spot's focal length and offset, simultaneously.

The pixel-based phased array and accompanying device test structures are also fabricated in a CMOS-compatible foundry process at CNSE SUNY on a 300-mm silicon-on-insulator (SOI) wafer with a 2- μm -thick buried oxide using 193 nm immersion lithography. However, a non-standard 380-nm-thick silicon

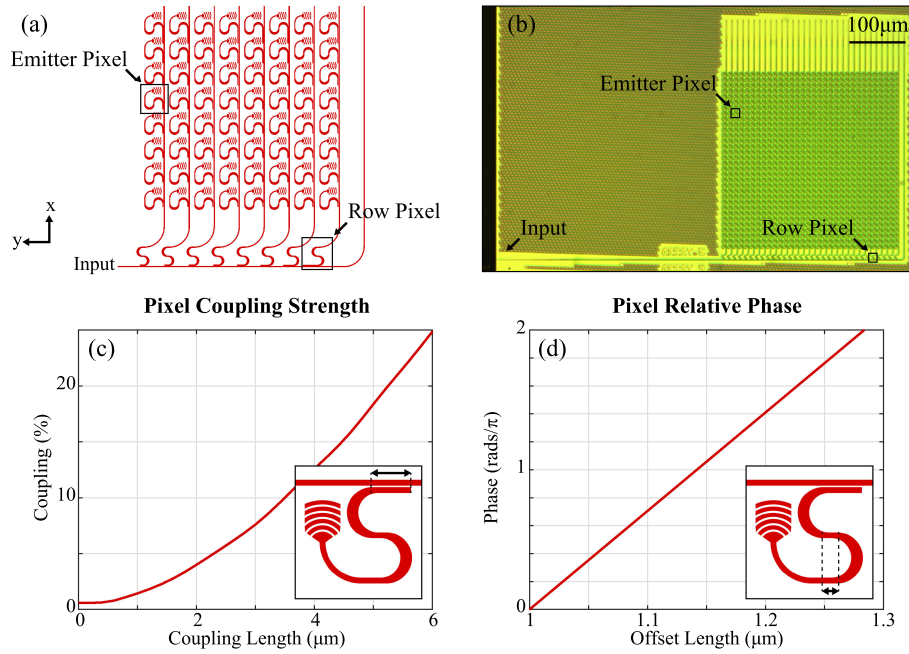


Fig. 6. (a) Schematic of a pixel-based focusing phased array with 64 antennas. (b) Micrograph of a fabricated pixel-based focusing phased array with 1024 antennas and 10 μm antenna pitch. Simulated (c) coupling versus coupling waveguide length and (d) relative phase versus offset length for the pixel-based architecture unit cell. Schematics of the unit cell are included as insets with each variable length indicated.

device layer is used (compared to the standard 220 nm thickness used in [5], [26]), which requires redesign of all photonic components in the system.

At the system input, an on-chip inverse-taper edge coupler is designed to efficiently couple light from a 6.5-μm-mode-field-diameter lensed fiber to a 450-nm-wide silicon waveguide with a ~2.5 dB measured coupling efficiency. A set of M row pixels are then used to couple light from the input waveguide to M row waveguides. Next, on each row waveguide, M emitter pixels are used to couple light from the row waveguide to M compact antenna emitters. This creates an array aperture of $M \times M$ antennas, as shown in Fig. 6(a). Notably, the row pixels and the emitter pixels are designed with the same topology (with the exception that the emitter pixels are terminated with antenna emitters) to enable arbitrary control of each antenna's amplitude and phase [5].

Within each row and emitter pixel, a directional coupler is used for amplitude control [5]. By increasing the length of the coupling region of the device, the percentage of power coupled either from the input waveguide to the row waveguide or from the row waveguide to the emitter is varied. Fig. 6(c) shows this relationship as simulated in FDTD assuming a 380 nm waveguide height and a 120 nm gap between the coupler and the waveguide. To enable uniform emission from each antenna within the array, the power coupling coefficients for both the row pixels and the emitter pixels are set to

$$\eta_m = \frac{1}{M - m + N_{\text{phantom}} + 1} \quad (5)$$

where η_m is the coupling coefficient for both the m th row pixel and the m th emitter pixel within each row, M is the total number of rows and the total number of emitters in each row, m

varies from 1 to M , and N_{phantom} is the number of desired “phantom” antennas [11], [26]. This phantom antenna concept is introduced to reduce the necessary coupling coefficient of the last pixel. Although this results in some power being discarded at the end of the input waveguide and each row waveguide, it eliminates the need for the last directional coupler to have 100% coupling, which would require a relatively long coupling length and increase the pixel size [26]. For example, in this implementation, N_{phantom} is set to 3 such that the highest coupling coefficient needed is 25%.

Each directional coupler is followed by two compact adiabatic curves with a variable offset length between them to allow for arbitrary phase control to each row or emitter [5]. Fig. 6(d) shows the resulting relative phase versus offset length as simulated in FDTD. For focusing in two dimensions, the offset lengths of each row and emitter pixel are set accordingly such that the correct phase profile, given by (3), is applied. Since the phase required for focusing in two dimensions is separable, the phases for focusing in each dimension can be independently applied – i.e., the phase profile for focusing in the y dimension is applied to the row pixels whereas the phase profile for focusing in the x dimension is applied to the emitter pixels. Additionally, the phase encodings are modified to compensate for the variable phase induced by the directional couplers as discussed in [26].

Finally, a compact emitter antenna is placed in each emitter pixel to radiate the light out of the plane of the chip at a slight angle from vertical to reduce back reflection. The emitter design is similar to the design presented in [5]; however, its dimensions are optimized for the custom 380-nm-height silicon. Specifically, each emitter antenna consists of 5 fully-etched grating teeth with a 490 nm period and a 172 nm gap between teeth.

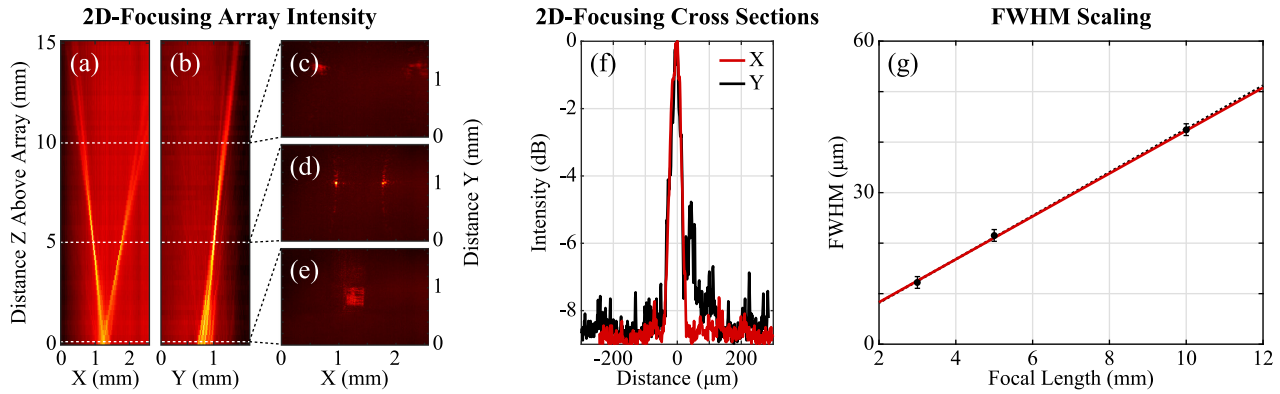


Fig. 7. Measured cross-sectional intensity (in dB) above the chip for a 5-mm-focal-length pixel-based phased array in the (a) x plane and (b) y plane with top-down intensity shown (e) in the plane of the chip, (d) at the focal plane, and (c) above the focal plane. (f) Measured cross-sectional intensity in x (red) and y (black) at the focal plane for the 5-mm-focal-length pixel-based phased array. (g) Simulated (red) and measured (black) power full-width half-maximum (FWHM) versus focal length. Results are shown for arrays with 1024 antennas, 10 μm antenna pitch, and 1550 nm wavelength.

To characterize the array, the same scanning optical imaging system is used as in Section III. The resulting cross-sectional intensity as a function of the distance above the chip and three top-down views are shown in Figs. 7(a)–(e) for the fabricated pixel-based 2D-focusing phased array with 1024 antennas (i.e., 32 rows by 32 columns), 10 μm antenna pitch, 5 mm focal length, and 1550 nm wavelength. Due to the 10 μm antenna pitch, multiple grating lobes are generated in the array factor in both the x and y dimensions. Two of these orders – the main beam and one of the first-order grating lobes – are seen in the camera’s field of view in the x dimension, as shown in Fig. 7(a). As the system scans to the focal plane 5 mm above the chip (Figs. 7(d) and 7(f)), the main beam is tightly focused, as expected. At this height, FWHMs of $\sim 21.5 \mu\text{m}$ are measured in both the x and y dimensions, closely matching the simulated value of 21.4 μm . Side-lobe suppressions of $\sim 8 \text{ dB}$ and $\sim 5 \text{ dB}$ are measured in the x and y dimensions, respectively (note that the noise floor in Fig. 7(f) is limited by the IR camera, not the array itself). Additionally, using a pinhole shutter at the focal plane to block any grating lobes and stray light and a detector above the shutter, an on-chip input to main lobe efficiency of approximately -18.5 dB is measured (the losses can be attributed to waveguide propagation loss, bending losses in the tight adiabatic bends, phantom antenna losses, and antenna emission losses, including power radiated to the grating lobes).

For comparison, two additional 1024-antenna pixel-based arrays are fabricated with 3 mm and 10 mm focal lengths. The measured FWHMs for all three arrays are plotted in Fig. 7(g) against the theory developed in Section II showing excellent agreement. As expected, the FWHM increases linearly with the focal length of the array.

Finally, a similar pixel-based array with 10,000 antennas (i.e., 100 rows by 100 columns) is fabricated. Since the aperture size of the array is significantly larger compared to the 1024 antenna array (1 mm \times 1 mm versus 0.32 mm \times 0.32 mm), the range of possible focal lengths is greatly increased due to the quadratic scaling of the near-field boundary compared to the aperture size. Similarly, the expected FWHMs are much smaller due to the inverse relationship of the aperture size and the FWHM.

As such, for the fabricated 10,000-antenna 10-mm-focal-length array, the measured FWHMs in the x and y dimensions are $\sim 23.3 \mu\text{m}$ and $\sim 20.9 \mu\text{m}$, respectively. However, due to the large number of antennas in the array, uniform distribution of power to each pixel in the array is more difficult since lower coupling coefficients and higher precision are needed. As such, these measured FWHMs are larger than the simulated value of 13.5 μm . In future implementations, lower coupling coefficients and higher precision could be achieved by varying the coupling gap, as proposed in [11], [26].

Similar to the splitter-tree-based architecture, since the pixel-based array is also fabricated in a CMOS-compatible platform, it is naturally scalable to a dynamic arbitrarily-tunable system with active silicon-based phase shifters integrated in each pixel as demonstrated in [5]. This extension of the system would enable both two-dimensional steering of the focal spot using the non-linear steering formulation developed in Section II and complete control of the focal length of the spot.

V. CONCLUSIONS, APPLICATIONS, AND FUTURE OUTLOOK

In summary, this work presents the first demonstration of integrated optical phased arrays that focus radiated light to a tightly-confined spot in the near field. The phase profiles necessary for generating focused beams using phased arrays with non-linear steering have been developed and relevant variables and parameters have been presented and discussed. Furthermore, two architectures have been proposed for demonstrating passive focusing integrated optical phased arrays: a one-dimensional splitter-tree-based architecture with focusing antennas and a two-dimensional pixel-based architecture. Both architectures have been used to demonstrate a variety of aperture size and focal length arrays, including a 512-antenna splitter-tree-based array with a $\sim 7 \mu\text{m}$ spot at a 5 mm focal length, a 1024-antenna pixel-based array with a $\sim 21 \mu\text{m}$ spot at a 5 mm focal length, and a 10,000-antenna pixel-based array with a $\sim 21 \mu\text{m}$ spot at a 10 mm focal length.

Since the arrays are fabricated in CMOS-compatible platforms, they are naturally scalable to active arbitrarily-tunable

systems with varying advantages. While the splitter-tree-based architecture is limited to active focusing in only one focal plane, it requires a smaller number of active controls and its close antenna pitch reduces the number of grating lobes, which increases the steering range of the device. In comparison, the pixel-based architecture enables control of the lateral steering and focal length in both dimensions and could be arbitrarily tuned without the need for a wavelength-tunable laser source; however, its large pixel pitch limits the steering range and it requires a larger number of active controls.

In addition to this natural evolution to active systems, the demonstrations can be scaled to larger aperture sizes [4] to further reduce the focal spot size and enable larger focal lengths. Additionally, to improve the field profile at the focal plane, both architectures can be modified to emit with Gaussian amplitude profiles by either using a star coupler for the splitter-tree-based architecture [8] or by modifying the coupling coefficients in the pixel-based architecture [7]. Furthermore, using numerical methods and synthesis algorithms [23], [24], the splitter-tree-based arrays can be further improved by appropriately varying the perturbation strength of the array's focusing antennas to produce either a uniform or a Gaussian emission profile. Finally, to improve the efficiencies of both architectures, the element-factor patterns of the long grating-based antennas and compact emitter antennas could be further optimized to reduce the power radiated to the grating lobes. Additionally, the pixel pitch of the pixel-based architecture could be reduced to lower the number of grating lobes by implementing a 1D splitting network with outputs that route to a 2D pixel-based emitter array [2]; however, this architecture would require individual phase control signals for each emitter to correctly apply the 2D-focusing phase.

The demonstrated on-chip focusing optical phased arrays have important applications in a variety of areas. For example, by enabling highly-enhanced tightly-focused beams with large focal lengths, these systems open up new possibilities for large-scale biological characterization and monitoring through optical trapping [13]–[15], especially for *in vivo* experiments wherein relatively large spatial offsets are an advantage [15]. Furthermore, by enabling a chip-based source of highly-focused beams, these devices have applications in chip-scale laser lithography techniques ranging from trapping-based nano-assembly [27], [28] to selective laser melting additive manufacturing [17].

ACKNOWLEDGMENT

The authors would like to thank M. J. Byrd and D. Vermeulen for coordinating the top-level mask assemblies. The devices demonstrated throughout this paper were fabricated at the Colleges of Nanoscale Science and Engineering (CNSE) at the SUNY Polytechnic Institute in Albany, New York, under the supervision of D. D. Coolbaugh, D. Coleman, C. Baiocco, and N. M. Fahrenkopf.

REFERENCES

- [1] C. V. Poulton *et al.*, "Coherent solid-state LiDAR with silicon photonic optical phased arrays," *Opt. Lett.*, vol. 42, no. 20, pp. 4091–4094, 2017.
- [2] F. Aflatouni, B. Abiri, A. Rekhi, and A. Hajimiri, "Nanophotonic projection system," *Opt. Express*, vol. 23, no. 16, pp. 21012–21022, 2015.

- [3] C. V. Poulton *et al.*, "Lens-free chip-to-chip free-space laser communication link with a silicon photonics optical phased array," *Frontiers Opt., Opt. Soc. Amer.*, 2017, pp. FW5A–3.
- [4] C. V. Poulton *et al.*, "Large-scale silicon nitride nanophotonic phased arrays at infrared and visible wavelengths," *Opt. Lett.*, vol. 42, no. 1, pp. 21–24, 2017.
- [5] J. Sun, E. Timurdogan, A. Yaacobi, E. S. Hosseini, and M. R. Watts, "Large-scale nanophotonic phased array," *Nature*, vol. 493, no. 7431, pp. 195–199, 2013.
- [6] S. Chung, H. Abediasl, and H. Hashemi, "A 1024-element scalable optical phased array in 0.18 μm SOI CMOS," in *Proc. IEEE Int. Solid-State Circuits Conf.*, 2017, pp. 262–263.
- [7] J. Sun *et al.*, "Two-dimensional apodized silicon photonic phased arrays," *Opt. Lett.*, vol. 39, no. 2, pp. 367–370, 2014.
- [8] D. N. Hutchison *et al.*, "High-resolution aliasing-free optical beam steering," *Optica*, vol. 3, no. 8, pp. 887–890, 2016.
- [9] T. Komljenovic, R. Helkey, L. Coldren, and J. E. Bowers, "Sparse aperiodic arrays for optical beam forming and LiDAR," *Opt. Express*, vol. 25, no. 3, pp. 2511–2528, 2017.
- [10] J. Hulme *et al.*, "Fully integrated hybrid silicon two dimensional beam scanner," *Opt. Express*, vol. 23, no. 5, pp. 5861–5874, 2015.
- [11] J. Zhou, J. Sun, A. Yaacobi, C. V. Poulton, and M. Watts, "Design of 3D hologram emitting optical phased arrays," in *Proc. Integr. Photon. Res., Silicon Nanophotonics.*, Opt. Soc. Amer., 2015, pp. IT4A.7.
- [12] J. Notaros, C. V. Poulton, M. J. Byrd, M. Raval, and M. R. Watts, "Integrated optical phased arrays for quasi-bessel-beam generation," *Opt. Lett.*, vol. 42, no. 17, pp. 3510–3513, 2017.
- [13] D. G. Grier, "A revolution in optical manipulation," *Nature*, vol. 424, no. 6950, pp. 810–816, 2003.
- [14] C. Bustamante, Z. Bryant, and S. B. Smith, "Ten years of tension: single-molecule DNA mechanics," *Nature*, vol. 421, no. 6921, pp. 423–427, 2003.
- [15] M.-C. Zhong, X.-B. Wei, J.-H. Zhou, Z.-Q. Wang, and Y.-M. Li, "Trapping red blood cells in living animals using optical tweezers," *Nature Commun.*, vol. 4, 2013, Art. no. 1768.
- [16] M. Endres *et al.*, "Atom-by-atom assembly of defect-free one-dimensional cold atom arrays," *Science*, vol. 354, pp. 1024–1027, 2016.
- [17] D. Gu, W. Meiners, K. Wissenbach, and R. Poprawe, "Laser additive manufacturing of metallic components: Materials, processes and mechanisms," *Int. Mater. Rev.*, vol. 57, no. 3, pp. 133–164, 2012.
- [18] J. A. Neff, R. A. Athale, and S. H. Lee, "Two-dimensional spatial light modulators: A tutorial," *Proc. IEEE*, vol. 78, no. 5, pp. 826–855, May 1990.
- [19] M. Khorasaninejad and F. Capasso, "Metalenses: Versatile multifunctional photonic components," *Science*, vol. 358, no. 6367, pp. eaam7100, 2017.
- [20] J. Notaros *et al.*, "CMOS-compatible optical phased arrays with monolithically-integrated erbium lasers," in *Proc. CLEO, Sci. Innovations.*, Opt. Soc. Amer., 2018, pp. STu4B–2.
- [21] E. Timurdogan *et al.*, "An ultra low power 3d integrated intra-chip silicon electronic-photonic link," in *Proc. Opt. Fiber Commun. Conf.*, Opt. Soc. Amer., 2015, pp. Th5B–8.
- [22] Y. Zhang *et al.*, "A compact and low loss y-junction for submicron silicon waveguide," *Opt. Express*, vol. 21, no. 1, pp. 1310–1316, 2013.
- [23] J. Notaros and M. A. Popović, "Finite-difference complex-wavevector band structure solver for analysis and design of periodic radiative microphotonic structures," *Opt. Lett.*, vol. 40, no. 6, pp. 1053–1056, 2015.
- [24] J. Notaros *et al.*, "Ultra-efficient CMOS fiber-to-chip grating couplers," in *Proc. Opt. Fiber Commun. Conf.*, Opt. Soc. Amer., 2016, p. M2I.5.
- [25] K. K. Mehta and R. J. Ram, "Precise and diffraction-limited waveguide-to-free-space focusing gratings," *Scientific Reports*, vol. 7, 2017, Art. no. 2019.
- [26] J. Sun *et al.*, "Large-scale silicon photonic circuits for optical phased arrays," *IEEE J. Sel. Topics Quantum Electron.*, vol. 20, no. 4, pp. 1–15, Jul./Aug. 2014.
- [27] P. J. Pauzauskie, A. Radenovic, E. Trepagnier, H. Shroff, P. Yang, and J. Liphardt, "Optical trapping and integration of semiconductor nanowire assemblies in water," *Nature Mater.*, vol. 5, no. 2, pp. 97–101, 2006.
- [28] S. H. Simpson and S. Hanna, "Holographic optical trapping of microrods and nanowires," *JOSA A*, vol. 27, no. 6, pp. 1255–1264, 2010.

Authors' biographies not available at the time of publication.